The Astrophysical Journal, 891:38 (13pp), 2020 March 1 https://doi.org/10.3847/1538-4357/ab6eff
© 2020. The American Astronomical Society. All rights reserved.

Rotational Desorption of Ice Mantles from Suprathermally Rotating Grains around Young Stellar Objects

Thiem Hoang[1,2] and Le Ngoc Tram[3,4]
[1] Korea Astronomy and Space Science Institute, Daejeon 34055, Republic of Korea; thiemhoang@kasi.re.kr
[2] University of Science and Technology, Korea, (UST), 217 Gajeong-ro Yuseong-gu, Daejeon 34113, Republic of Korea
[3] SOFIA-USRA, NASA Ames Research Center, MS 232-11, Moffett Field, CA 94035, USA
[4] University of Science and Technology of Hanoi, VAST, 18 Hoang Quoc Viet, Hanoi, Vietnam
Received 2019 October 13; revised 2020 January 16; accepted 2020 January 21; published 2020 March 2

Abstract

Ice mantles on dust grains play a central role in astrochemistry. Water and complex organic molecules (COMs) are thought to first form on the ice mantles and subsequently are released into the gas phase due to star-formation activity. However, the critical question is whether ice mantles can survive stellar radiation when grains are being heated from $T_d \sim 10$ K to $\gtrsim$100 K. In this paper, we first study the effect of suprathermal grain rotation driven by the intense radiation of young stellar objects on the ice mantles. We find that the entire ice mantles can be disrupted into small fragments by centrifugal stress before the water ice and COMs desorb via thermal sublimation. We then study the consequence of resulting ice fragments and find that tiny fragments of radius $a \lesssim 10$ Å exhibit a transient release of COMs due to thermal spikes, whereas larger fragments can facilitate thermal sublimation at much higher rates than from the original icy grain, or the same rate but with temperatures of ∼20–40 K lower. We find that rotational desorption is efficient for hot cores/corinos from the inner to outer regions where the temperature drops to $T_{\rm gas} \sim 40$ K and $n_{\rm H} \sim 10^4$ cm^{-3}. We discuss the implications of this mechanism for desorption of COMs and water ice in various environments, including outflow cavity walls, photodissociation regions, and protoplanetary disks. Finally, we show that very large aggregate grains can be disrupted into individual icy grains via a rotational disruption mechanism, followed by rotational desorption of ice mantles.

Unified Astronomy Thesaurus concepts: Interstellar dust (836); Dense interstellar clouds (371); Molecule formation (2076); Interstellar molecules (849); Molecule destruction (2075); Astrochemistry (75); Star formation (1569); Protostars (1302)

1. Introduction

Water molecules are essential for life, and complex organic molecules (COMs; referring to organic molecules containing ⩾6 atoms, such as CH_3OH, CH_3OCH_3, $HCOOCH_3$, and C_2H_5OH, CH_3CH_2CN), are the building blocks of life. Understanding where and how such molecules are formed and released into the gas phase is a key question in astrochemistry. COMs are increasingly observed in the environs of young stellar objects (YSOs), including hot cores/corinos around high-mass/low-mass protostars and protoplanetary disks (PPDs) (see Herbst & van Dishoeck 2009 and van Dishoeck 2014 for recent reviews). In the formation process of water and COMs, the ice mantle of dust grains is known to play a central role (see van Dishoeck 2014, 2017 for recent reviews).

The popular scenario for forming COMs in hot cores/corinos involves three phases, including cold, warm, and hot phases (Herbst & van Dishoeck 2009). During the initial cold phase, COMs may first be formed in the cold molecular core (Jimenez-Serra et al. 2016) but are frozen in the icy grain mantle during the cloud collapse process (zeroth-generation species). During the warm phase, i.e., after star formation, the ice mantle is warmed up from ∼10 K to ∼100 K by protostellar radiation, which increases the mobility of simple molecules frozen in the ice mantle and finally form COMs (first-generation species; see, e.g., Garrod et al. 2008). During the hot phase where icy grain mantles are heated to 100–300 K, thermal sublimation of ice mantles (Blake et al. 1987; Brown et al. 1988; Bisschop et al. 2007) can release molecules (CH_3OH, NH_3), which trigger gas-phase chemistry at high temperatures and form in situ COMs (second-generation species; see Charnley et al. 1992).

Given the crucial importance of the icy grain mantles on the formation and desorption of water and COMs, the remaining question is whether the ice mantles can still survive in the intense radiation field of YSOs during the warm phase when thermal sublimation is not yet effective.

Previous research on the thermal and non-thermal desorption of molecules from the grain mantle assumed that grains are at rest, which is contrary to the fact that grains are rapidly rotating due to collisions with gas atoms and interstellar photons (Draine & Lazarian 1998; Hoang et al. 2010). To understand how molecules form on the grain surfaces and are returned to the gas, the effect of grain rotation of gas-grain chemistry must be quantified. The goal of this paper is to quantify the effect of grain rotation on the desorption of ice mantles from the grain surface.

Interstellar dust grains are widely known to be rotating suprathermally, as required to reproduce starlight polarization and far-IR/submillimeter polarized dust emission (see Andersson et al. 2015 and Lazarian et al. 2015 for reviews). Indeed, Purcell (1979) first suggested that dust grains can be spun up to suprathermal rotation (with velocities larger than grain thermal velocity) by various mechanisms, including the formation of hydrogen molecules on the grain surface.

In particular, modern astrophysics establishes that dust grains of irregular shapes can rotate suprathermally due to radiative torques (RATs) arising from their interaction with an anisotropic radiation field (Draine & Weingartner 1996;

Lazarian & Hoang 2007a; Hoang & Lazarian 2008, 2009; Herranen et al. 2019) or mechanical torques induced by an anisotropic gas flow (Lazarian & Hoang 2007b; Hoang et al. 2018a). In an intense radiation field, Hoang et al. (2019) discovered that irregular grains could be spun up to extremely fast rotation such that the centrifugal stress can exceed the tensile strength of the grain material, breaking the original grain into many fragments. This mechanism of grain destruction is termed radiative torque disruption (RATD). Therefore, in star-forming regions and photodissociation regions (PDRs), we expect that the radiation intensity is sufficiently intense such that the centrifugal force can disrupt the ice mantle from the grain core into small icy fragments. Consequently, sublimation from such tiny fragments would occur at a much higher rate than from the original large grain. This issue will be quantified in the present paper.

The structure of the paper is as follows. In Section 2 we will introduce the rotational desorption mechanism of ice mantles from suprathermally rotating dust grains spun up by RATs due to centrifugal stress. We will demonstrate that the resulting small fragments can induce faster evaporation of COMs than classical thermal sublimation in Section 3. In Section 4, we apply rotational desorption mechanism for hot cores/corinos around protostars. Discussion for other environments, including PDRs and PPDs, and the effect of grain evolution for rotational desorption are presented in Section 5. Major findings are summarized in Section 6.

2. Rotational Desorption Mechanism of Icy Grain Mantles

2.1. Ice Mantles on Grain Surface

The formation of an ice mantle due to accretion of gas molecules on the grain surface is expected to occur in cold and dense regions of hydrogen density $n_{\rm H} = n({\rm H}) + 2n({\rm H_2}) \sim 10^3$–$10^5\,{\rm cm^{-3}}$ or the visual extinction $A_V > 3$ (Whittet et al. 1983). Ice mantles on the grain surface are expected to have layer structures because water and CO condense at different temperatures, where the first layer is dominated by water ice and the second layer is dominated by CO ice (see Oberg et al. 2010). The detection of strongly polarized H_2O and CO ice absorption features (Chrysostomou et al. 1996; Whittet et al. 2008) demonstrates that icy grain mantles have non-spherical shape and are aligned with magnetic fields (see Lazarian et al. 2015 for a review).

The mantle thickness can vary with the size of dust grains due to their difference in grain temperature (see Pauly & Garrod 2016). In dense clouds, one expects the ice mantle to have ∼100 monolayers on large grains ($a \gtrsim 0.1\,\mu$m) and about 30–50 monolayers on small grains, assuming gas density $n_{\rm H} \sim 10^4\,{\rm cm^{-3}}$. At high densities of $\sim 10^7\,{\rm cm^{-3}}$, the ice mantle can grow to ∼380 monolayers after ∼1 Myr (Garrod & Pauly 2011).

Here we consider a grain model consisting of an amorphous silicate core covered by a double-layer ice mantle (see Figure 1). Let a_c be the radius of silicate core and Δa_m be the average thickness of the mantle. The exact shape of icy grains is unknown, but we can assume that they have irregular shapes as required by polarization data (Chrysostomou et al. 1996). Thus, one can define an effective radius of the grain, a, which is defined as the radius of the sphere with the same volume as the grain. The effective grain size is $a \approx a_c + \Delta a_m$. The silicate and carbonaceous core perhaps are assumed to have a typical radius of 0.05 μm (Greenberg 1989). In the following, we first assume the maximum size of core-mantle grains is $a_{\rm max} \sim 1\,\mu$m and postpone discussion of grain growth to Section 5.

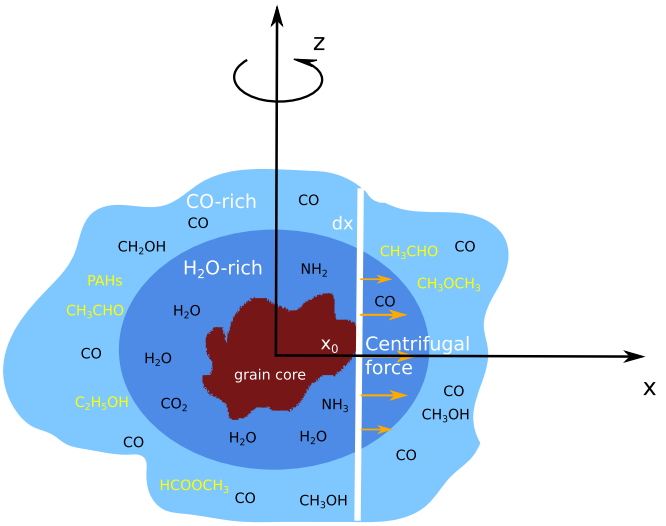

Figure 1. A schematic illustration of a rapidly spinning core-mantle grain of irregular shape, comprising icy water-rich (blue), and CO-rich (orange) mantle layers. The core is assumed to be compact silicate material, and complex organic molecules are formed in the ice mantle of the core. Centrifugal force field on a slab dx is illustrated, which acts to pull off the ice mantle from the grain core at sufficiently fast rotation.

2.2. Suprathermal Rotation of Dust Grains by RATs

We consider an anisotropic radiation field of the anisotropy degree γ. Let u_λ be the spectral energy density of radiation field at wavelength λ. The energy density of the radiation field is then $u_{\rm rad} = \int u_\lambda d\lambda$. To describe the strength of a radiation field, lets define $U = u_{\rm rad}/u_{\rm ISRF}$ with $u_{\rm ISRF} = 8.64 \times 10^{-13}\,{\rm erg\,cm^{-3}}$ being the energy density of the average interstellar radiation field (ISRF) in the solar neighborhood, as given by Mathis et al. (1983). Thus, the typical value for the ISRF is $U = 1$. Let $\overline{\lambda} = \int \lambda u_\lambda d\lambda / u_{\rm rad}$ be the mean wavelength of the radiation field. For the ISRF, $\overline{\lambda} \sim 1.2\,\mu$m (Draine & Weingartner 1997).

As shown in Hoang et al. (2019), for the radiation source of constant luminosity, i.e., constant RAT, $\Gamma_{\rm RAT}$ (Draine & Weingartner 1996; Lazarian & Hoang 2007a), the grain angular velocity is steadily increased over time as

$$\omega(t) = \omega_{\rm RAT}\left[1 - \exp\left(-\frac{t}{\tau_{\rm damp}}\right)\right], \quad (1)$$

where

$$\omega_{\rm RAT} = \frac{\Gamma_{\rm RAT}\tau_{\rm damp}}{I} \quad (2)$$

is the terminal angular velocity at time much larger than damping time, $t \gg \tau_{\rm damp}$, which is considered the maximum rotational rate spun up by RATs (Hoang et al. 2019).

Above, $\tau_{\rm damp} = t_{\rm gas}^{-1} + \tau_{\rm IR}^{-1} = \tau_{\rm gas}^{-1}(1 + F_{\rm IR})$ is the total damping rate where $t_{\rm gas}$ is the rotational damping time due to gas collisions, and $F_{\rm IR}$ is the grain rotational damping coefficient due to infrared emission (see Draine & Lazarian 1998). For a gas with He of 10% abundance, the

characteristic damping time due to collisions is

$$\tau_{\rm gas} = \frac{3}{4\sqrt{\pi}}\frac{I}{1.2 n_{\rm H} m_{\rm H} v_{\rm th} a^4} \simeq 8.74 \times 10^4 a_{-5}\hat{\rho}\left(\frac{30\ {\rm cm}^{-3}}{n_{\rm H}}\right)\left(\frac{100\ {\rm K}}{T_{\rm gas}}\right)^{1/2}\ {\rm yr}, \quad (3)$$

where $a_{-5} = a/(10^{-5}\ {\rm cm})$, $\hat{\rho} = \rho/(3\ {\rm g\ cm}^{-3})$ with ρ being the dust mass density, $v_{\rm th} = (2k_{\rm B}T_{\rm gas}/m_{\rm H})^{1/2}$ is the thermal velocity of gas atoms of mass $m_{\rm H}$ in a plasma with temperature $T_{\rm gas}$ and density $n_{\rm H}$, and spherical grains are assumed (Draine & Weingartner 1996; Hoang & Lazarian 2009).

For grains in thermal equilibrium due to starlight heating and radiative cooling, one obtains (see Draine & Lazarian 1998)

$$F_{\rm IR} \simeq \left(\frac{0.4U^{2/3}}{a_{-5}}\right)\left(\frac{30\ {\rm cm}^{-3}}{n_{\rm H}}\right)\left(\frac{100\ {\rm K}}{T_{\rm gas}}\right)^{1/2}. \quad (4)$$

Following Hoang (2019), the maximum rotation rate of grains spun up by RATs is given by

$$\omega_{\rm RAT} \simeq 9.6 \times 10^8 \gamma a_{-5}^{0.7}\bar{\lambda}_{0.5}^{-1.7} \times \left(\frac{U}{n_1 T_2^{1/2}}\right)\left(\frac{1}{1+F_{\rm IR}}\right){\rm rad\ s}^{-1}, \quad (5)$$

for grains with $a \leqslant \bar{\lambda}/1.8$, and

$$\omega_{\rm RAT} \simeq 1.78 \times 10^{10} \gamma a_{-5}^{-2}\bar{\lambda}_{0.5} \times \left(\frac{U}{n_1 T_2^{1/2}}\right)\left(\frac{1}{1+F_{\rm IR}}\right){\rm rad\ s}^{-1}, \quad (6)$$

for grains with $a > \bar{\lambda}/1.8$. Above, $n_1 = n_{\rm H}/(10\ {\rm cm}^{-3})$, $T_2 = T_{\rm gas}/(100\ {\rm K})$, and $\bar{\lambda}_{0.5} = \bar{\lambda}/(0.5\ \mu{\rm m})$. The rotation rate depends on the parameter $U/n_{\rm H}T_{\rm gas}^{1/2}$ and $F_{\rm IR}$. For $U \gg 1$, $\omega_{\rm RAT}$ is much larger than the thermal angular velocity of grains $\omega_T = (2kT_{\rm gas}/I)^{1/2} \sim 2 \times 10^5 a_{-5}^{-5/2}T_2^{1/2}{\rm rad\ s}^{-1}$, which is referred to as suprathermal rotation.

For convenience, let $a_{\rm trans} = \bar{\lambda}/1.8$, which denotes the grain size at which the RAT efficiency changes between the power law and flat stages (see e.g., Lazarian & Hoang 2007a; Hoang et al. 2019), and $\omega_{\rm RAT}$ changes from Equations (5) to (6).

We note that the RAT efficiency weakly depends on the composition of dust grains as shown in Lazarian & Hoang (2007a) and Herranen et al. (2019). Thus, Equations (5) and (6) can be applicable for both silicate and carbonaceous grains.

2.3. Rotational Desorption of Ice Mantles

2.3.1. Centrifugal Stress and Tensile Strength of Ice Mantles

It is assumed that the grain is rotating around the axis of maximum inertia moment, denoted by z-axis, with angular velocity ω. This assumption is valid for suprathermal rotating grains in which internal relaxation can rapidly induce the perfect alignment of the axis of the major inertia with the angular momentum, which corresponds to the minimum rotational energy state (Purcell 1979). Let us consider a slab dx at distance x from the center of mass. The average tensile stress due to centrifugal force dF_c acting on a plane located at distance x_0 is equal to

$$dS = \frac{\omega^2 x dm}{\pi(a^2 - x_0^2)} = \frac{\rho_{\rm ice}\omega^2(a^2-x^2)xdx}{a^2 - x_0^2}, \quad (7)$$

where the mass of the slab $dm = \rho_{\rm ice}dAdx$ with $dA = \pi(a^2 - x^2)$ the area of the circular slab, $\rho_{\rm ice}$ is the mass density of the ice mantle, which is $\rho_{\rm ice} \sim 1\ {\rm g\ cm}^{-3}$ for pure ice.

The surface average tensile stress is then given by

$$S_x = \int_{x_0}^{a} dS_x = \frac{\rho_{\rm ice}\omega^2 a^2}{2}\int_{x_0/a}^{1}\frac{(1-u)du}{1-u_0} = \frac{\rho_{\rm ice}\omega^2 a^2}{4}\left(\frac{(1-u_0)^2}{1-u_0}\right) = \frac{\rho_{\rm ice}\omega^2 a^2}{4}\left[1 - \left(\frac{x_0}{a}\right)^2\right], \quad (8)$$

where $u = x^2/a^2$.

Equation (8) reveals that the tensile stress is maximum at the grain center and decreases with decreasing the mantle thickness $(a - x_0)$.

By plugging the numerical numbers into Equation (8), one obtains

$$S_x \simeq 2.5 \times 10^9 \hat{\rho}_{\rm ice}\omega_{10}^2 a_{-5}^2\left[1 - \left(\frac{x_0}{a}\right)^2\right]{\rm erg\ cm}^{-3}, \quad (9)$$

where $\hat{\rho}_{\rm ice} = \rho_{\rm ice}/(1\ {\rm g\ cm}^{-3})$ and $\omega_{10} = \omega/(10^{10}{\rm rad\ s}^{-1})$.

The tensile strength of the bulk ice is $S \sim 2 \times 10^7\ {\rm erg\ cm}^{-3}$ at low temperatures. As the temperature increases to 200–300 K, the tensile strength is reduced significantly to $5 \times 10^6\ {\rm erg\ cm}^{-3}$ (Litwin et al. 2012). The adhesive strength between the ice mantle and the solid surface has a wide range, depending on the surface properties (Itagaki 1983; Work & Lian 2018). Here, we adopt a conservative value of $S_{\rm max} = 10^7\ {\rm erg\ cm}^{-3}$ for ice mantles for our numerical calculations. For the grain core, a higher value of $S_{\rm max} = 10^9\ {\rm erg\ cm}^{-3}$ is adopted.

When the rotation rate is sufficiently high, such that the tensile stress exceeds the maximum limit of the ice mantle, $S_{\rm max}$, the grain is disrupted. The critical rotational velocity is determined by $S_x = S_{\rm max}$:

$$\omega_{\rm disr} = \frac{2}{a(1 - x_0^2/a^2)^{1/2}}\left(\frac{S_{\rm max}}{\rho_{\rm ice}}\right)^{1/2} \simeq \frac{6.3 \times 10^8}{a_{-5}(1 - x_0^2/a^2)^{1/2}}\hat{\rho}_{\rm ice}^{-1/2}S_{\rm max,7}^{1/2}\ {\rm rad\ s}^{-1}, \quad (10)$$

where $S_{\rm max,7} = S_{\rm max}/(10^7\ {\rm erg\ cm}^{-3})$.

Although the detail of rotational disruption of dust grains is not yet studied, the disruption process perhaps undergoes the following steps. When the grain rotation rate is increased to the critical disruption limit, the ice mantle near the equator is detached because the centrifugal stress is equal to the tensile strength of the mantle onto the grain core. As the rotation rate is further increased beyond $\omega_{\rm disr}$, the centrifugal stress exceeds the ice tensile strength that holds the different parts of the mantle together, resulting in the disruption of the mantle into small fragments.

Above, we assume that the grain is spinning along the principal axis of maximum inertia moment. This assumption is valid because internal relaxation within the rapidly spinning grain due to Barnett effect rapidly brings the grain axis to be

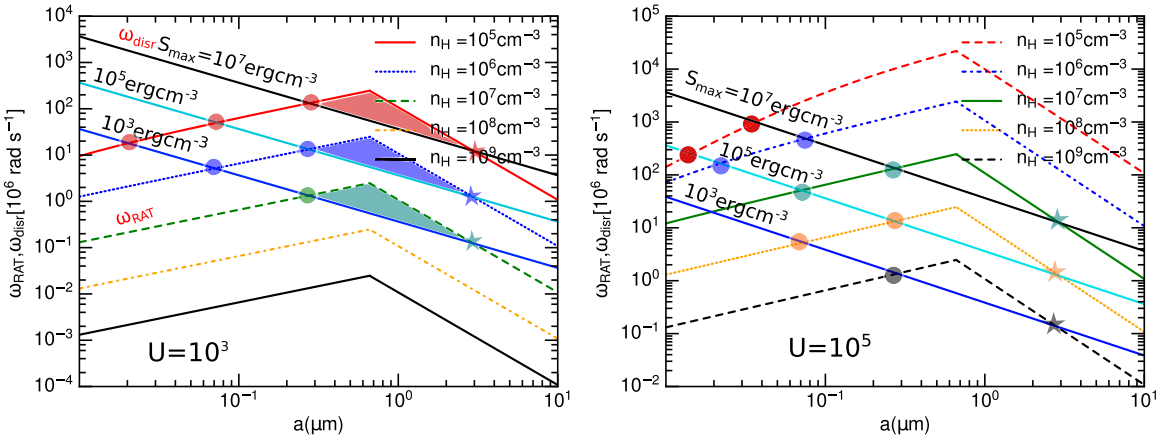

Figure 2. Grain rotation rate spun up by RATs ($\omega_{\rm RAT}$) and disruption rate ($\omega_{\rm disr}$) as functions of the grain size for different gas densities. Two values of the radiation strength $U = 10^3$ (left panel) and $U = 10^5$ (right panel) and three values of tensile strengths $S_{\rm max} = 10^3$, 10^5, 10^7 erg cm^{-3} are considered. The peak of $\omega_{\rm RAT}$ occurs at $a = a_{\rm trans}$. The intersection of $\omega_{\rm RAT}$ and $\omega_{\rm disr}$ can occur at a lower grain size (marked by a circle) and an upper size (marked by a star), and the shaded area denotes the range of grain sizes in which grains are disrupted by RATs.

aligned with its angular momentum (Purcell 1979; Roberge & Lazarian 1999).

2.3.2. Desorption Sizes of Ice Mantles

The critical grain size of rotational desorption can be found by setting $\omega_{\rm RAT} = \omega_{\rm disr}$. From Equations (5)–(6) and (10), one can see that when the grain size increases, $\omega_{\rm RAT}$ rapidly increases and then intersects with $\omega_{\rm disr}$ at $a = a_{\rm disr}$, assuming sufficiently strong radiation fields. When the grain size continues to increase beyond $a_{\rm trans}$, $\omega_{\rm RAT}$ then declines rapidly as $\propto a^{-2}$ and then intersects $\omega_{\rm disr} \propto a^{-1}$ again at some large grain size, producing a second intersection. The first intersection determines the critical size above which grains are disrupted, whereas the second intersection determines the maximum size that grains still can be disrupted.

Figure 2 shows the rotation rate versus disruption rate for different gas densities, tensile strengths, assuming the radiation strength of $U = 10^3$ and 10^5. The intermediate strength of $S_{\rm max} \sim 10^5$ erg cm^{-3} is expected for composite grains (Hoang 2019; see Gundlach et al. 2018 for experimental results). The intersection between $\omega_{\rm RAT}$ and $\omega_{\rm disr}$ occurs at a lower grain size ($a_{\rm disr}$) and a very large grain size ($a_{\rm disr,max}$). The range $[a_{\rm disr} - a_{\rm disr,max}]$ describe the sizes of grains that are rotationally disrupted, which is referred to as the disruption size range. When the disruption size is smaller than $a_{\rm trans}$, the disruption size range becomes broader. On the other hand, when the disruption size $a_{\rm disr} \to a_{\rm trans}$, the disruption size range is reduced to $a = a_{\rm trans}$.

The grain size at the first intersection can be obtained from Equations (5) and (10), which is given by

$$a_{\rm disr} \simeq 0.13\gamma^{-1/1.7}\bar{\lambda}_{0.5}(S_{\rm max,7}/\hat{\rho}_{\rm ice})^{1/3.4} \times (1+F_{\rm IR})^{1/1.7}\left(\frac{n_1 T_2^{1/2}}{U}\right)^{1/1.7} \mu{\rm m}, \quad (11)$$

for $a_{\rm disr} \lesssim a_{\rm trans}$ and $x_0 \ll a$, which depends on the local gas density and temperature due to gas damping. The equation indicates that all grains in the size range $a_{\rm trans} > a > a_{\rm disr}$ would be disrupted.

To determine the maximum size of grains that can still be disrupted by centrifugal stress, one needs to compare $\omega_{\rm RAT}$ from Equation (6) with $\omega_{\rm disr}$, which yields

$$a_{\rm disr,max} \simeq 2.9\gamma\bar{\lambda}_{0.5}\left(\frac{U}{n_1 T_2^{1/2}}\right)\left(\frac{1}{1+F_{\rm IR}}\right)\hat{\rho}_{\rm ice}^{1/2} S_{\rm max,7}^{-1/2}\ \mu{\rm m}. \quad (12)$$

For the standard parameters of the diffuse interstellar medium, one gets $a_{\rm disr,max} \sim 2.9\ \mu$m for the typical physical parameters in Equation (12). This is much larger than the maximum grain size of $a_{\rm max} \sim 0.25$–$0.3\ \mu$m obtained from modeling of observational data (Mathis et al. 1977; Kim & Martin 1995; Draine & Fraisse 2009). So, all available grains of $a \gtrsim a_{\rm disr}$ are disrupted. In dense regions, grains are expected to grow to large sizes due to coagulation and accretion (e.g., Chokshi et al. 1993; Ossenkopf 1993). Therefore, not all grains of $a \gtrsim a_{\rm disr}$ can be disrupted, and we will find both $a_{\rm disr}$ and $a_{\rm disr,max}$ for grains in star-forming regions. Due to dependence of $F_{\rm IR}$ on the grain size and S_x on x_0, one must find $a_{\rm disr}$ and $a_{\rm disr,max}$ using numerical calculations instead of Equations (11) and (12).

Note that calculations of RATs for irregular shapes are limited to grains of size $a < \lambda/0.1$ (Lazarian & Hoang 2007a; Herranen et al. 2019). Therefore, the actual maximum disruption size might be lower than given by Equation (12) if $a_{\rm disr,\ max} > \lambda/0.1$ because RATs of such very large grains are expected to decrease due to random effects when different photons scan the different facets of the grain.

2.3.3. Desorption Time of Ice Mantles

In the absence of rotational damping, the characteristic timescale for rotational desorption can be estimated as

$$t_{\rm disr,0} = \frac{I\omega_{\rm disr}}{dJ/dt} = \frac{I\omega_{\rm disr}}{\Gamma_{\rm RAT}} \simeq 0.6(\gamma U_5)^{-1}\bar{\lambda}_{0.5}^{1.7}\hat{\rho}_{\rm ice}^{1/2} S_{\rm max,7}^{1/2} a_{-5}^{-0.7}\ {\rm yr} \quad (13)$$

for $a_{\rm disr} < a \lesssim a_{\rm trans}$, and

$$t_{\rm disr,0} \simeq 0.04(\gamma U_5)^{-1}\bar{\lambda}_{0.5}^{-1}\hat{\rho}_{\rm ice}^{1/2} S_{\rm max,7}^{1/2} a_{-5}^{2}\ {\rm yr} \quad (14)$$

for $a_{\rm trans} < a < a_{\rm disr,max}$ where $U_5 = U/10^5$.

Table 1
Disruption Size of Ice Mantles from the Grain with Fixed Core Radius $a_c = 0.05\ \mu$m

Gas Density		$a_{\rm disr}(\mu{\rm m})$			
$n_{\rm H}$(cm^{-3})	$U = 10^3$	10^4	10^5	10^6	10^7
	T_d(K) ≈ 52	76	112	164	240
10^5	0.2597	0.0849	0.0525	0.0506	0.0249
10^6	ND[a]	0.2680	0.0921	0.0522	0.0303
10^7	ND	ND	ND	0.0979	0.0528
10^8	ND	ND	ND	ND	0.1092

Note.
[a] ND: no disruption.

In the presence of rotational damping, the disruption timescale can be obtained by solving $\omega(t) = \omega_{\rm disr}$, which yields

$$t_{\rm disr} = -\tau_{\rm damp}\ln\left(1 - \frac{\omega_{\rm disr}}{\omega_{\rm RAT}}\right) = -\tau_{\rm damp}\ln\left(1 - \frac{t_{\rm disr,0}}{\tau_{\rm damp}}\right), \quad (15)$$

which is applicable for $a_{\rm disr,max} > a > a_{\rm disr}$. Note that $t_{\rm disr} \to \infty$ for $a = [a_{\rm disr}, a_{\rm disr,max}]$ because it takes $t \gg t_{\rm damp}$ to reach $\omega = \omega_{\rm RAT}$. One see that $t_{\rm disr}$ returns to $t_{\rm disr,0}$ when $t_{\rm disr,0} \ll \tau_{\rm damp}$ which is achieved in strong radiation fields.

3. Rotational Desorption of Ice Mantles and Subsequent Evaporation

In this section, we will use the theory from the previous section to quantify the rotational desorption of ice mantles into tiny icy fragments. We then demonstrate that the subsequent evaporation of molecules from resulting icy fragments is much faster than the evaporation from the original icy mantle grain.

3.1. Rotational Desorption Size of Ice Mantles

We consider a unidirectional radiation field (i.e., $\gamma = 1$) in which dust grains are illuminated by a central YSO and consider two different mean wavelengths of the radiation field $\bar{\lambda} = 0.5$ and $1.2\ \mu$m (e.g., typical interstellar radiation). Specifically, we consider a range of gas density $n_{\rm H} \sim 10^5$–$10^9\ {\rm cm}^{-3}$ and radiation strength $U \sim 10^3 - 10^8$ around YSOs. Due to such dense conditions, the gas and dust grain temperatures (of large grains $a = 0.1\ \mu$m) are similar. The value of $a_{\rm disr,max}$ is set to $a_{\rm max} = 1\ \mu$m in the absence of the intersection between $\omega_{\rm RAT}$ and $\omega_{\rm disr}$.

We first consider a core-mantle grain model with a fixed core radius $a_{\rm c} = 0.05\ \mu$m, and the mantle thickness can vary.

Table 1 shows the disruption size of the ice mantle from a core-mantle grain for selected physical parameters and the radiation field of $\bar{\lambda} = 0.5\ \mu$m, assuming a fixed core radius $a_c = 0.05\ \mu$m.

Figure 3 shows the range of grain disruption sizes ($a_{\rm disr}$, $a_{\rm disr,max}$) as functions of the radiation strength U for the different gas density, assuming $\bar{\lambda} = 0.5\ \mu$m (panel (a)) and $\bar{\lambda} = 1.2\ \mu$m (panel (b)). The shaded regions mark the parameter space (a, U)) where the rotational disruption occurs. One can see that $a_{\rm disr}$ decreases rapidly and $a_{\rm disr,max}$ increases linearly with the radiation strength U (panels (a) and (b)). This reveals the range of the disruption size is broadened with increasing U.

The disruption size decreases rapidly with increasing U and then slowly approaches $a_{\rm c}$ when the centrifugal stress on the interface between the core and the mantle decreases to zero. The latter determines the lower boundary of rotational desorption determined by the strong grain core.

We now assume that icy mantles of the same thickness cover all grain cores of the different sizes (a_c) and adopt the thickness $\Delta a_m = 0.05\ \mu$m. Results are shown in Figure 5. We find that the disruption size is essentially the same for $a > a_{\rm c}$. The results are similar to those in Figures 3 and 4, but the lower boundary is shifted to the corresponding value of a_c. Furthermore, the ice mantles on larger grain cores are desorbed at lower temperatures than from smaller grain cores, which originates from the increase of RATs with the grain size.

To easily compare rotational desorption with sublimation, in Figure 4, we show the desorption sizes as a function of the grain temperature, where

$$T_d \simeq 16.4 a_{-5}^{-1/15} U^{1/6}\ {\rm K} \quad (16)$$

for silicate grains (Draine 2011).

For dense regions of density of $n_{\rm H} \sim 10^5$–$10^6\ {\rm cm}^{-3}$, a thick mantle of $a \sim 1\ \mu$m can be removed first at $T_d = 80$ K. When the temperature increases to 100 K, the mantle layer has been removed until the grain radius is reduced to $\sim$0.1 μm and can be removed. For higher density of $n_{\rm H} \sim 10^8\ {\rm cm}^{-3}$, the ice mantle starts to be separated at $T_d \sim 100$ K, and the entire mantle is completely removed at $T_d \sim 200$ K. For very dense regions of $n_{\rm H} \sim 10^7\ {\rm cm}^{-3}$, one sees the ice mantle destruction is very efficient starting from $T_d \sim 100$ K. In extremely dense regions of $n_{\rm H} \sim 10^9\ {\rm cm}^{-3}$, stronger radiation intensity with $T_d \gtrsim 250$ K can still disrupt ice mantles.

We now consider a core-ice mantle model in which the mantle thickness is fixed to $\Delta a_m = 0.025\ \mu$m and $0.05\ \mu$m, and the grain core radius r_c is varied. Results are shown in Figure 5. The desorption of the thicker mantle tends to occur at lower grain temperatures. Compared to Figure 4, one can see that the ice mantle desorption requires higher radiation strength/temperature to be efficient. This feature originates from the fact that thicker ice mantles induce larger tensile stress acting on the interface between the mantle and the grain core (see Equation (9)), which decreases the critical rotation rate and then requires a lower strength of ambient radiation fields.

3.2. Rotational Desorption Time Versus Sublimation Time

We calculate the desorption time of ice mantles for the different grain temperatures, assuming the different grain sizes and a fixed mantle thickness of $\Delta a_m = 0.05\ \mu$m. Obtained results are shown in Figure 6.

For comparison, we also compute the sublimation time of the ice mantle, as given by

$$t_{\rm sub}(T_d) = -\frac{\Delta a_m}{da/dt} = \frac{\Delta a_m}{l\nu_0}\exp\left(\frac{E_b}{T_d}\right), \quad (17)$$

where $da/dt = l/\tau_{\rm evap}$ is the rate of decrease in the mantle thickness due to thermal sublimation, l is the thickness of the ice monolayer, and $\tau_{\rm evap}$ is the characteristic time that

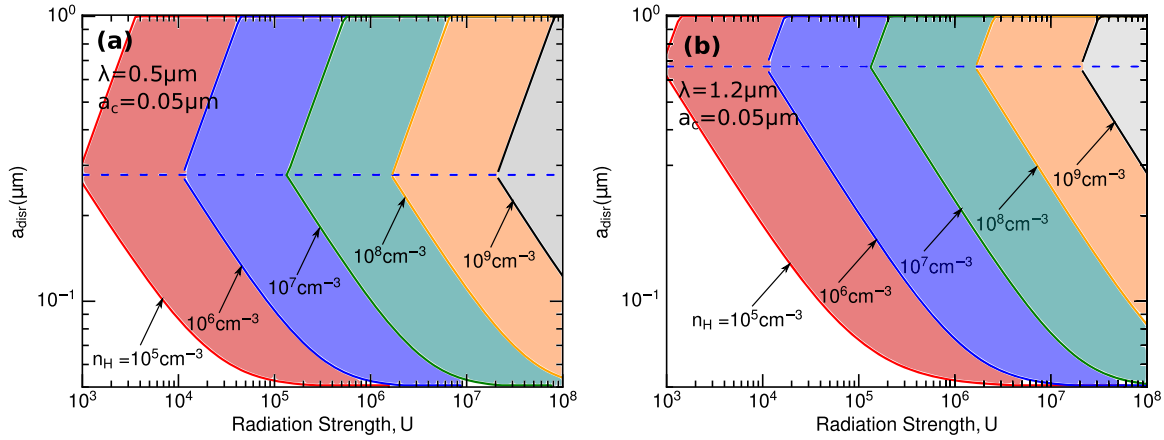

Figure 3. Range of desorption sizes of ice mantles, constrained by $a_{\rm disr}$ (lower boundary) and $a_{\rm disr,max}$ (upper boundary), as a function of the grain temperature for the different gas densities for $\bar{\lambda} = 0.5\ \mu$m (panel (a)) and $\bar{\lambda} = 1.2\ \mu$m (panel (b)), assuming a fixed core radius a_c and the varying mantle thickness. The horizontal dashed lines denote the transition size $a_{\rm trans} = \bar{\lambda}/1.8$. Shaded regions mark the range of grain sizes disrupted by RATD.

molecules stay on the grain surface before evaporation:

$$\tau_{\rm evap}^{-1} = \nu_0 \exp\left(\frac{-E_b}{T_d}\right), \quad (18)$$

where ν_0 is the characteristic vibration frequency of the lattice, and E_b is the binding energy (Watson & Salpeter 1972). Table 2 lists the binding energy and sublimation temperatures from experiments of the different molecules.

Plugging the numerical parameters of water ice into the above equation, we obtain

$$t_{\rm sub} \sim 1.5 \times 10^3 \left(\frac{\Delta a_m}{500\ \text{Å}}\right) \exp\left(\frac{E_b}{4800\ \text{K}} \frac{100\ \text{K}}{T_d}\right) \text{yr}. \quad (19)$$

Comparing Equation (19) with (13) one can see that rotational desorption is much faster than thermal sublimation of water ice at $T_d \sim 100$ K.

Results for $t_{\rm sub}$ of several molecules with large binding energies, including H_2O, CH_3OH, HCOOH, C_2H_5OH, and $(CH_2OH)_2$, are shown in Figure 6. We adopt the characteristic frequency $\nu_0 = 5 \times 10^{12}\ \text{s}^{-1}$ (see e.g., Hasegawa & Herbst 1993). The disruption time is smaller for larger grain sizes, but it increases when $a > a_{\rm trans}$. Below the sublimation temperature (i.e., temperatures of 50–100 K), rotational desorption is faster than sublimation for densities of $n_{\rm H} \lesssim 10^6\ \text{cm}^{-3}$. At densities of $n_{\rm H} \sim 10^7\ \text{cm}^{-3}$, rotational desorption is faster than sublimation of water ice at $T \sim 100$–120 K (i.e., below sublimation limit of water ice). At higher density $n_{\rm H} \sim 10^8\ \text{cm}^{-3}$, rotational desorption is faster than sublimation of ethanol for $T \sim 130$–160 K.

3.3. Rapid Evaporation of COMs and Water Ice From Tiny Fragments

Below we will study the subsequent evaporation of COMs and water ice from tiny fragments produced by rotational desorption of ice mantles.

A detailed study about the size distribution of fragments resulting from rotational desorption of ice mantles is beyond the scope of this paper. Nevertheless, we can assume that resulting fragments include nanoparticles and tiny clusters of molecules (i.e., very small icy grains). The maximum size of fragments is perhaps comparable to the thickness of ice mantle of ~25 nm (i.e., 250 Å). The remaining question is how rapidly COMs and water ice can evaporate from such icy fragments.

Since icy fragments are exposed to the same strong stellar radiation as original large grains, due to low heat capacity, they can be rapidly heated to higher temperatures than the original grain (see Draine & Li 2001 for more details). Indeed, the absorption of a single UV photon can instantaneously raise the temperature of the fragment to

$$T_{\rm VSG} = \frac{\Delta E}{C_{\rm V}}, \quad (20)$$

where ΔE is the energy that a UV photon transfers to the dust grain, $C_{\rm V} = 3N_{at}k_B$ is the volume heat capacity of the ice fragment, and $N_{at} = 4/3\pi a^3 n_{\rm ice}$ is the total number of atoms. The number density of atoms in the pure water ice mantle is $n_{\rm ice} \sim \rho_{\rm ice}/m(H_2O) \approx 3.3 \times 10^{22}\ \text{cm}^{-3}$.

The temperature of icy fragments can be rewritten as

$$T_{\rm VSG} \simeq 276 \left(\frac{E}{10\ \text{eV}}\right)\left(\frac{a}{1\ \text{nm}}\right)^{-3} \text{K}. \quad (21)$$

It follows that for $a \lesssim 1$ nm, single-photon absorption can transiently heat the fragment to $T_{\rm VSG} \gtrsim 270$ K, which exceeds the thermal sublimation threshold of COMs (see Table 2). In general, one expects a fraction of tiny fragments below 1 nm, therefore, COMs and water ice can rapidly evaporate following the rotational desorption of ice mantles.

Larger fragments of $a \sim 1$–25 nm can achieve equilibrium temperatures due to radiative heating, and their temperatures are considerably higher than that of original large grains of $a \sim 0.1\ \mu$m, as given by Equation (16). Due to a steep dependence of the sublimation rate on the grain temperature, a moderate increase in the temperature of small fragments can significantly increase the sublimation rate of COMs from these small fragments. Indeed, for $U \sim 10^5$, one has $T_d \sim 111.7$ K for $a = 0.1\ \mu$m, and $T_d \sim 130.2$ K for $a = 0.01\ \mu$m. The ratio of their sublimation rates is equal to

$$\frac{\tau_{\rm sub}(a = 0.01\ \mu\text{m})^{-1}}{\tau_{\rm sub}(a = 0.1\ \mu\text{m})^{-1}} \sim \frac{\exp(-4800/130.2)}{\exp(-4800/111.7)} \sim 450. \quad (22)$$

Figure 7 (upper panel) shows the sublimation time for three different grain sizes as a function of the temperature of $a = 0.1\ \mu$m grains. For a given temperature, the sublimation rate of smaller grains is several orders of magnitude larger than

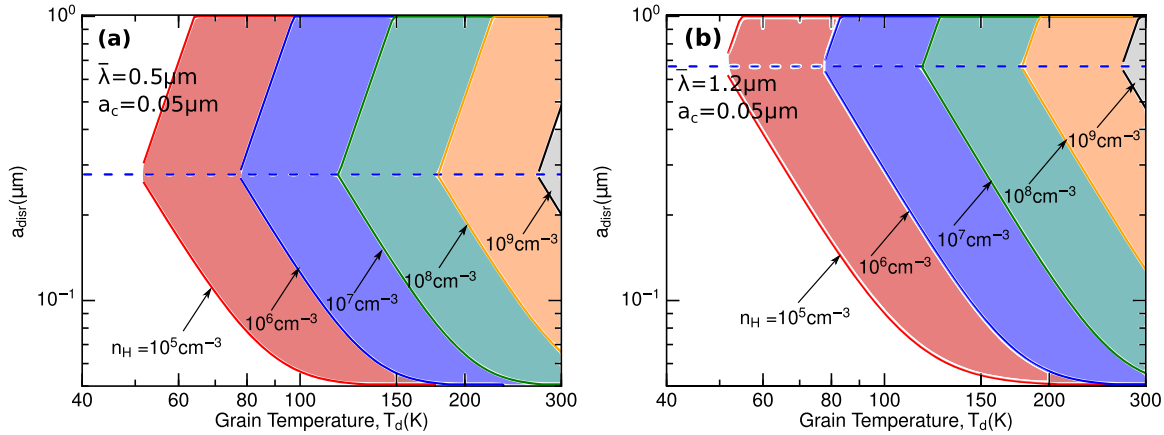

Figure 4. Same as Figure 3, but for the dependence of grain temperature. At density of $n_{\rm H} \sim 10^5\,{\rm cm}^{-1}$, the ice mantle is removed at $T_d \gtrsim 60$ K, but at higher density $n_{\rm H} \sim 10^6\,{\rm cm}^{-3}$, the ice mantle is substantially removed only when $T_d \gtrsim 100$ K.

that of large grains. Therefore, by disrupting the ice mantle on a large grain into small fragments, rotational desorption can allow the sublimation of COMs and water ice at a much faster rate compared to the original icy grain mantle.

Figure 7 (lower panel) shows the decrease of grain temperature to have the same sublimation rate as a function of grain sizes. The decrease of grain temperature decreases rapidly with the fragment size and achieves $|\delta T| \gtrsim 20$ K for $a \lesssim 0.01\,\mu$m.

To summarize the rotational desorption mechanism introduced in this section, in Figure 8, we illustrate the rotational desorption process of COMs from icy grain mantles which includes two stages. First, the ice mantle of a large core-ice mantle grain ($a_c = 0.1\,\mu$m) is disrupted into small fragments by means of RATD. Second, very small fragments ($a \lesssim 1$ nm) are transiently heated to high temperatures, inducing transient evaporation of molecules. Larger fragments (e.g., $a \sim 1$–10 nm) can be heated to higher temperatures than the original grain, which significantly enhances the rate of thermal sublimation as shown in Figure 7.

4. Application: Rotational Desorption of Ice Mantles in Hot Cores/Corinos

We now apply our theory in the previous section to study the desorption of ice mantles from grains in hot cores and hot corinos, which are inner regions surrounding high-mass protostars (Blake et al. 1987) and low-mass protostars (Bottinelli et al. 2004; Beltran & Rivilla 2018).

Hot cores/corinos are directly heated by the central protostar. Let L be the bolometric luminosity of the protostar. The radiation strength at distance r from the source is given by

$$U(r) = \left(\frac{L}{4\pi r^2 c u_{\rm ISRF}}\right) = U_{\rm in}\left(\frac{r_{\rm in}}{r}\right)^2, \quad (23)$$

where $U_{\rm in}$ denotes the radiation strength at inner radius $r_{\rm in}$.

The gas density and temperature can be approximately described by power laws

$$n_{\rm gas} = n_{\rm in}\left(\frac{r_{\rm in}}{r}\right)^p, \quad (24)$$

$$T_{\rm gas} = T_{\rm in}\left(\frac{r_{\rm in}}{r}\right)^q, \quad (25)$$

where $n_{\rm in}$ and $T_{\rm in}$ are gas density and temperature at radius $r_{\rm in}$, and $q = 2/(4+\beta)$ with β the dust opacity index (see e.g., Chandler & Richer 2000). The typical density profile in the inner hot region is $p \sim 1.5$. A more detailed model of hot cores is presented in Nomura & Millar (2004).

From Equation (11), one obtains the disruption size of ice mantles as follows

$$a_{\rm disr}(r) \simeq 0.13\gamma^{-1/1.7}\bar{\lambda}_{0.5}(S_{\rm max,7}/\hat{\rho}_{\rm ice})^{1/3.4}\,(1+F_{\rm IR})^{1/1.7} \times \left(\frac{n_{\rm in}T_{\rm in}^{1/2}}{100U_{\rm in}}\right)^{1/1.7}\left(\frac{r_{\rm in}}{r}\right)^{(p+q/2-2)/1.7}\,\mu{\rm m}, \quad (26)$$

which slowly decreases with radius r as $r^{(p+q/2-2)/1.7} \sim r^{-0.1}$ for typical slopes.

For low-mass protostars, one can assume $r_{\rm in} = 25$ au and $n_{\rm in} \sim 10^8\,{\rm cm}^{-3}$ and $L = 36L_\odot$ (Visser et al. 2012), one gets $a_{\rm disr} \sim 0.29\,\mu$m at $r = r_{\rm in}$ and $a_{\rm disr} \sim 0.63\,\mu$m for $r = 10r_{\rm in}$. For hot cores, we adopt a typical luminosity of $L = 10^5L_\odot$ and typical parameters $r_{\rm in} \sim 500$ au, $n_{\rm in} \sim 10^8\,{\rm cm}^{-3}$, $U_{\rm in} \sim 2\times10^7$, and $T_{\rm in} \sim 274$ K (see e.g., Bisschop et al. 2007). Therefore, Equation (26) gives $a_{\rm disr} = 0.1\,\mu$m and $0.16\,\mu$m at $r = r_{\rm in}$, $10r_{\rm in}$, respectively. The results for $n_{\rm in} = 10^7\,{\rm cm}^{-3}$ as usually assumed (Viti & Williams 1999) are even more promising.

Figure 9 illustrates the importance of rotational desorption versus classical thermal sublimation of ice mantles around a protostar of $L = 10^5L_\odot$ and $\bar{\lambda} = 0.5\,\mu$m. Thermal evaporation is important only in the inner regions where $T_{\rm gas} > 100$ K, whereas rotational desorption can be efficient at larger radii with low temperatures of $T_{\rm gas} \sim 40$–100 K.

We note that even in the hot inner region where thermal sublimation is active, rotational desorption and ro-thermal desorption (Hoang & Tung 2019) are more efficient than the classical sublimation for molecules with high binding energy such as water and COMs.

The efficiency of rotational desorption in cold extended regions shown in Figure 9 successfully explains the presence of COMs from outer extended regions around hot cores by Fayolle et al. (2015). Furthermore, this mechanism can explain the presence of HCOOH, CH_3CHO from cold regions with $T_{\rm gas} \sim 40$–70 K (below the sublimation threshold of these molecules) and low column density by Bisschop et al. (2007).

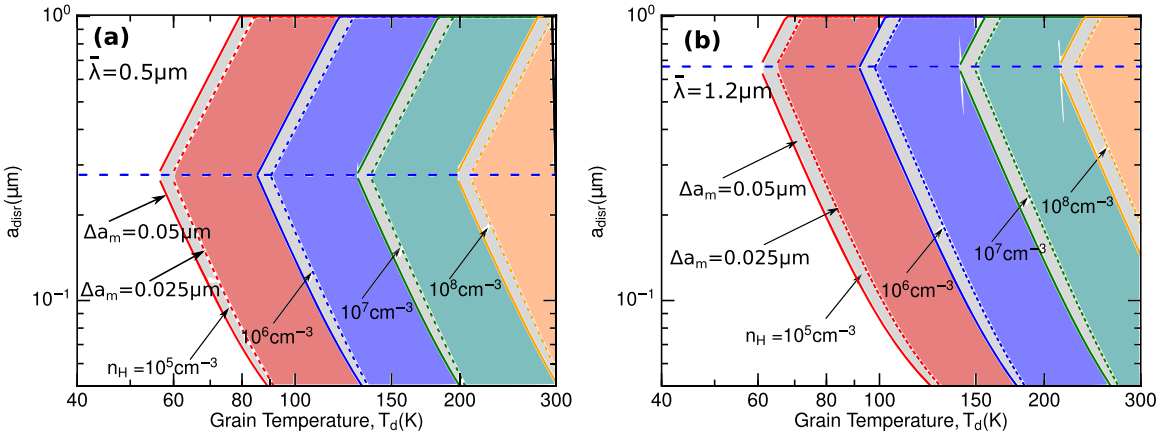

Figure 5. Same as Figure 4, but for the model with a fixed mantle thickness of $\Delta a_m = 0.05\ \mu$m (solid lines) and 0.025 μm (dashed lines). For $n_{\rm H} \sim 10^5\ {\rm cm}^{-1}$, the ice mantle is removed at $T_d \gtrsim 60$ K, but for higher density $n_{\rm H} \sim 10^6\ {\rm cm}^{-3}$, the ice mantle is removed only when $T_d \gtrsim 100$ K.

Future high-resolution observations by the Atacama Large Millimeter/submillimeter Array (ALMA) would be unique to test our prediction of an extended region of COMs.

5. Discussion

5.1. Comparison of Rotational Desorption with Other Desorption Mechanisms in Star-forming Regions

First of all, we should stress that in this paper we are primarily concerned with the desorption of molecules in star-forming regions where icy grains are illuminated by protostars and quantify an important physical effect, namely, suprathermal rotation of grains, which is disregarded in previous studies.

Both rotational desorption and thermal sublimation of COMs from ice mantles rely on interaction of radiation fields with dust grains to be efficient. Here, we outline the key differences of the rotational desorption mechanism that can be tested with observations.

From Figure 6 one can see that rotational desorption can occur at low temperatures below the sublimation threshold of COMs and water ice, and the critical temperature for rotational desorption decreases with decreasing the local gas density (Hoang et al. 2019; see also Section 6). It can be effective even at temperatures of $T < 50$ K if the local gas density is $n_{\rm H} < 10^5\ {\rm cm}^{-3}$. Therefore, COMs/water vapor can be observed in cold regions ($T < 100$ K) with not very high gas density. On the other hand, thermal sublimation only depends on the grain temperature, which requires intense radiation so that grains can be heated to $T > 100$ K.

Second, compared to classical sublimation, the circumstellar region in which rotational desorption is important would be more extended due to lower required radiation intensity. For instance, using $U \sim T_d^6$, one can estimate the radius of regions in which rotational desorption is efficient as $R_{\rm desr}/R_{\rm sub} = (U_{\rm sub}/U_{\rm desr})^{1/2} \sim (T_{\rm sub}/T_{\rm desr})^3 \sim (100/80)^3 \sim 2$. Therefore, we predict that COMs can be released in a region more extended than classical sublimation by a factor of 2.

Third, through rotational desorption, COMs and water ice can be released simultaneously from tiny fragments ($a < 1$ nm). For larger fragments ($a \sim 1$ nm $- \Delta a_m$), the sublimation is essentially a classical one but with significantly enhanced rates, and COMs of the different binding energies are released at the different distances from the radiation source.

Finally, while photodesorption requires far-UV photons ($h\nu \gtrsim 6$ eV or $\lambda < 0.2\ \mu$m) to be effective (Oberg et al. 2009), rotational desorption can work with a broad range of the radiation spectrum (i.e., $\lambda > 0.2\ \mu$m) because RATs depend on the ratio of the photon wavelength to the grain size (Lazarian & Hoang 2007a; Herranen et al. 2019). Let us estimate the lifetime of an icy grain by UV photodesorption. Let $Y_{\rm pd}$ be the photodesorption yield of water ice, which is defined as the fraction of molecules ejected over the total number of incident UV photons. The rate of mass loss due to UV photodesorption is

$$\frac{dm}{dt} = \frac{4\pi a^2 \rho_{\rm ice} da}{dt} = \bar{m} Y_{\rm pd} F_{\rm FUV} \pi a^2, \tag{27}$$

where $\bar{m}$ is the mean mass of ejected molecules, $F_{\rm FUV}$ is the flux of FUV photons. Let $G_0 = F_{\rm FUV}/F_{\rm FUV,ISRF}$ be the strength of the UV photons relative to the standard ISRF. Then, the above equation becomes

$$\frac{da}{dt} = 2.2 \times 10^{-3} G_0 \left(\frac{Y_{\rm pd}}{0.001}\right) \text{Å yr}^{-1}, \tag{28}$$

where $\bar{m} = m({\rm H_2O})$ and the typical yield $Y_{\rm pd} = 0.001$ (Oberg et al. 2009) is adopted.

Using the typical parameters for a hot core, one obtains the photodesorption time for an ice mantle of thickness Δa_m:

$$t_{\rm pd} = \frac{\Delta a_m}{da/dt} \simeq \left(\frac{\Delta a_m(\text{ Å})}{2.2 \times 10^{-3}\ \text{Å}}\right)\left(\frac{10^{-3}}{Y_{\rm pd}}\right)\left(\frac{1}{G_0}\right)\ \text{yr}$$
$$\simeq 2.2\left(\frac{\Delta a_m}{500\ \text{Å}}\right)\left(\frac{10^{-3}}{Y_{\rm pd}}\right)\left(\frac{10^5}{G_0}\right)\text{yr}. \tag{29}$$

Comparing $t_{\rm pd}$ with $t_{\rm disr}$ (Equation (13)) one can see that the rotational disruption is one order of magnitude faster than UV photodesorption, assuming $G_0 \sim U_0 \sim 10^5$ and $a = 0.1\ \mu$m. In the shielded region of optical depth τ_V, the UV strength is reduced to $G = G_0 e^{-\tau_{\rm FUV}}$, but the optical radiation is reduced to $U = U_0 e^{-\tau_V}$ only where $\tau_{\rm FUV} \sim 2 - 3\tau_V$ (see e.g., Weingartner & Draine 2001). The UV photodesorption yield of methanol is found to be very low, $<10^{-6}$ (Bertin et al. 2016), although this yield only takes into account intact methanol molecules. One important aspect is that the penetration length of FUV photons is much shorter than optical photons due to higher dust

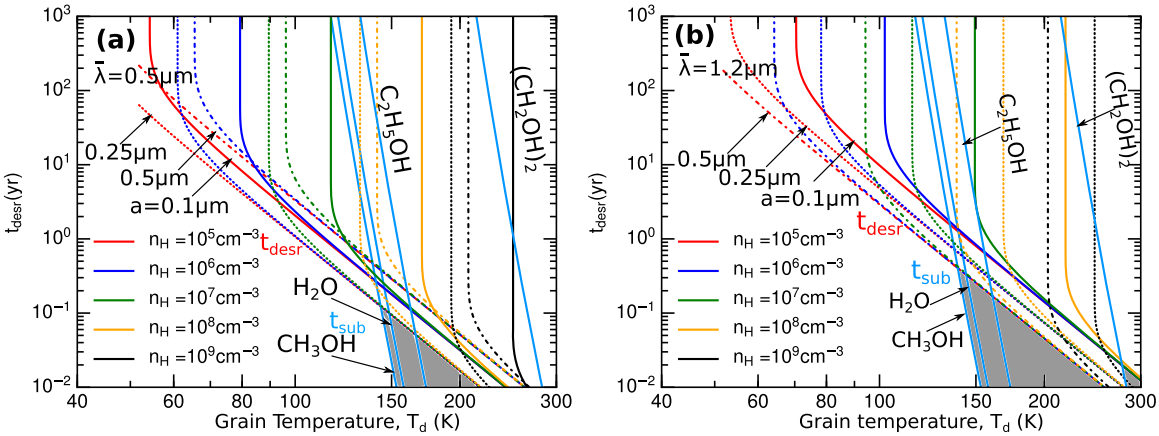

Figure 6. Desorption time vs. grain temperature for the different grain sizes (a = 0.1, 0.25, 0.5 μm). Thermal sublimation time of several popular COMs and water for a mantle thickness Δa_m = 0.025 μm is shown for comparison. Rotational desorption occurs faster than thermal sublimation and requires lower grain temperatures. Gray shaded areas mark the region where thermal sublimation is faster.

Table 2
Binding Energies and Sublimation Temperatures for Selected Molecules on an Ice Surface

Molecules	E_b (K)[a]	T_{sub} (K)
H_2O	5700	152[b]
CH_3OH	5530	99[b]
HCOOH	5570	155[c]
CH_3CHO	2775	30[c]
C_2H_5OH	6260	250[c]
$(CH_2OH)_2$	10,200	350[c]
NH_3	5530	78[b]
CO_2	2575	72[b]
H_2CO	2050	64[b]
CH_4	1300	31[b]
CO	1150	25[b]

Notes.
[a] See Table 4 in Garrod (2013).
[b] See Table 1 from Mumma et al. (1993).
[c] See Collings et al. (2004).

extinction. As a result, rotational desorption is efficient in more extended regions around YSOs than photodesorption.

5.2. Rotational Desorption Enhances Abundance of COMs in the Outflow and the Outflow Cavity Walls of Protostars and PDRs

Due to the clearing-out by outflows, stellar radiation can freely propagate through the outflow cavity (of gas density $n_H \sim 10^3$ cm^{-3}) and illuminate icy grains in the cavity wall (boundary region between outflow and envelope). The cavity wall behaves like a photodominated region where the radiation strength can be larger than $U \sim 10^3$–10^4, and the gas density of the outflow cavity wall is $n_H \sim 10^4$–10^6 cm^{-3} (Visser et al. 2012). With these physical parameters, using the results from Figure 5, one can see that the entire mantle can be evaporated via rotational desorption, which increases the abundance of COMs in the cavity wall.

Rotational desorption of ice mantles is also expected to increase the abundance of COMs in the outflows of protostars because of high radiation intensity and low gas density. Indeed, observations usually show an enhancement of COMs in the outflows of low-mass protostars (Drozdovskaya et al. 2015) and high-mass protostar (Palau et al. 2017). COMs are also observed to be more abundant in the shock L1157-B1 than in hot corinos (Lefloch et al. 2017). We note that Drozdovskaya

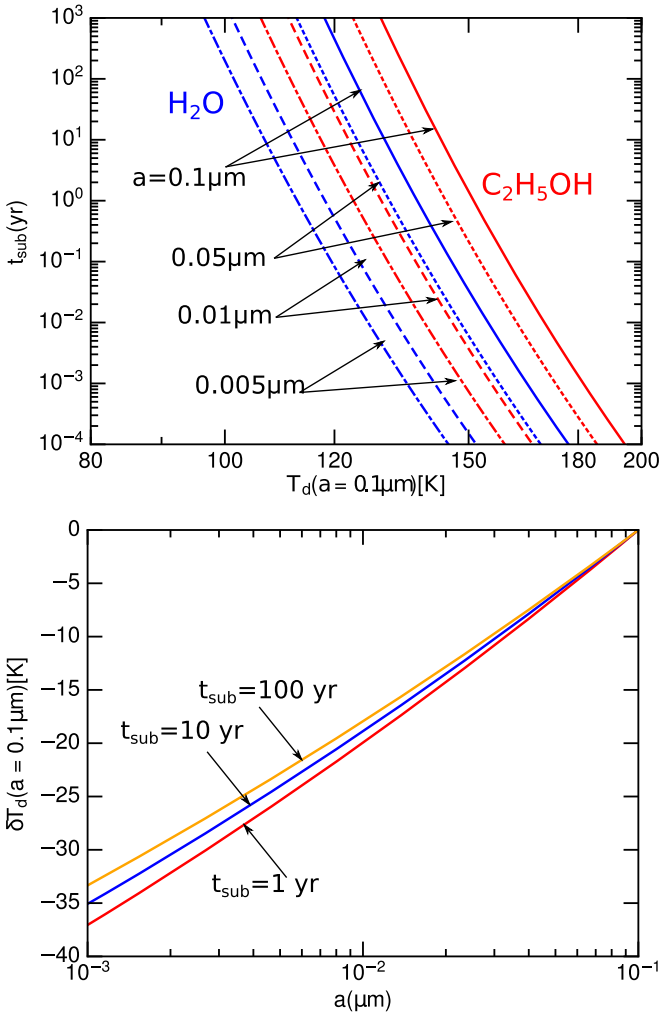

Figure 7. Upper panel: thermal sublimation time of water ice and ethanol vs. the temperature of 0.1 μm grains for the different sizes. The sublimation time is significantly decreased with decreasing the grain radius. Lower panel: the decrease of grain temperature required to produce the same sublimation rate vs. grain size, assuming t_{sub} = 1, 10, 100 yr.

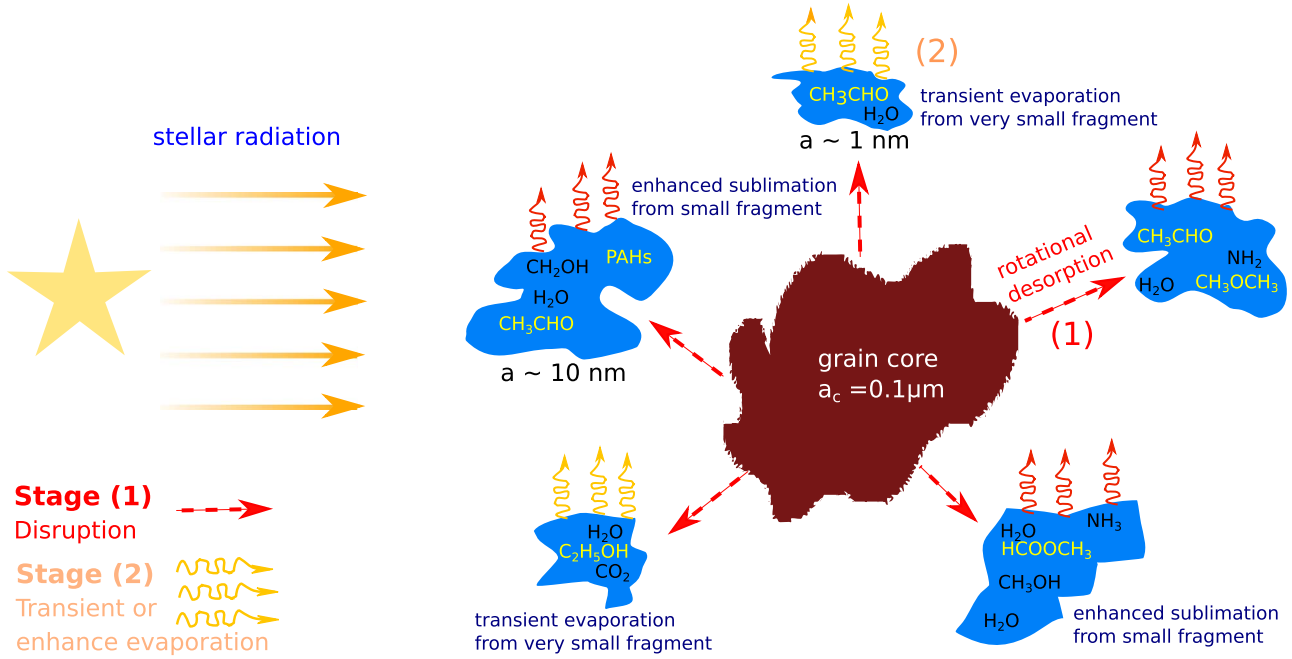

Figure 8. Schematic illustration of rotational desorption process of COMs from icy grain mantles comprising two stages: (1) disruption of icy mantes into small fragments by RATD, and (2) rapid evaporation of COMs due to thermal spikes for very small fragments or increased sublimation for larger fragments.

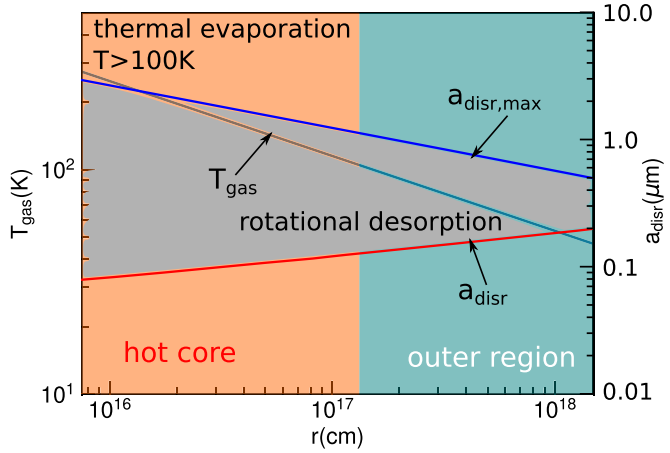

Figure 9. Gas temperature and grain disruption size vs. radius for an envelope around a high-mass protostar. Classical thermal sublimation is important only for the inner region (hot core), whereas rotational desorption is important for both the hot core and outer region.

et al. (2015) explained the enhancement of COMs by means of UV irradiation from protostars due to the outflow cavity (see also Karska et al. 2014). Yet, an enhanced irradiation would increase the efficiency of photodestruction of COMs. Palau et al. (2017) explained this enhancement due to sputtering and grain–grain collisions in C-shocks of velocities $v < 40$ km s^{-1} in the cavity walls. However, a recent work by Godard et al. (2019) shows that C-shocks shrink in the radiation fields of $G_0 > 0.2(n_{\rm H}/1\ {\rm cm}^{-3})^{1/2}$, which would reduce the efficiency of sputtering.

At far distances from the protostar, the effect of shocks can be important. As shown in Hoang & Tram (2019) and Tram & Hoang (2019), C-shocks can spin up nanoparticles to suprathermal rotation due to supersonic drift of neutrals relative to charged grains. Then, icy grain mantles can be released, producing gas-phase COMs by either the rapid disruption of weak nanoparticles, or rotational desorption of strong nanoparticles (Tram & Hoang 2019).

Finally, rotation desorption of ice mantles is important for PDRs, which are dense ($n_{\rm H} \sim 10^4$–10^5 cm^{-3}) and directly illuminated by strong stellar radiation of $U \sim 10^3$–10^5. We note that outflow cavity walls and surface of circumstellar disk are also considered PDRs (Spaans et al. 1995). Thus, rotational desorption is expected to be efficient in releasing COMs from icy mantles for these PDR environments. Using the results in Figure 5, one can see that the icy mantles can be rapidly removed from $a \gtrsim 0.2$ μm grains. This mechanism can explain the detection of COMs and polycyclic aromatic hydrocarbons in PDRs (see Cuppen et al. 2017 for a review).

5.3. Effect of Grain Evolution on Grain-surface Chemistry: Link Between Dust Properties and COMs

Our numerical results presented in Section 2 are also obtained for core-ice mantle grains with the maximum size of $a_{\rm max} \sim 1$ μm, and the typical grain size adopted for chemical modeling of gas-grain chemistry is $a = 0.1$ μm (see e.g., Garrod 2013). However, in dense prestellar cores and PPDs, grain coagulation due to grain–grain collisions is expected to form large fluffy aggregates of original icy grains, namely composite grains (Ossenkopf & Henning 1994; Hirashita & Li 2013). Various observations show the signature of grain growth in prestellar cores (Pagani et al. 2010) and young protostellar systems (Kwon et al. 2009). Note that in dense molecular clouds where interstellar radiation is significantly attenuated, coagulation of icy grains can proceed to form large aggregates, without being rotationally disrupted by RATD. However, when exposed to strong radiation of protostars/young stars, such large composite grains are expected to be destroyed via the RATD mechanism (Hoang et al. 2019).

The disruption of large grains can also be calculated using the method in Section 2, but with the tensile strength of composite grains (Greenberg et al. 1995; Li & Greenberg 1997;

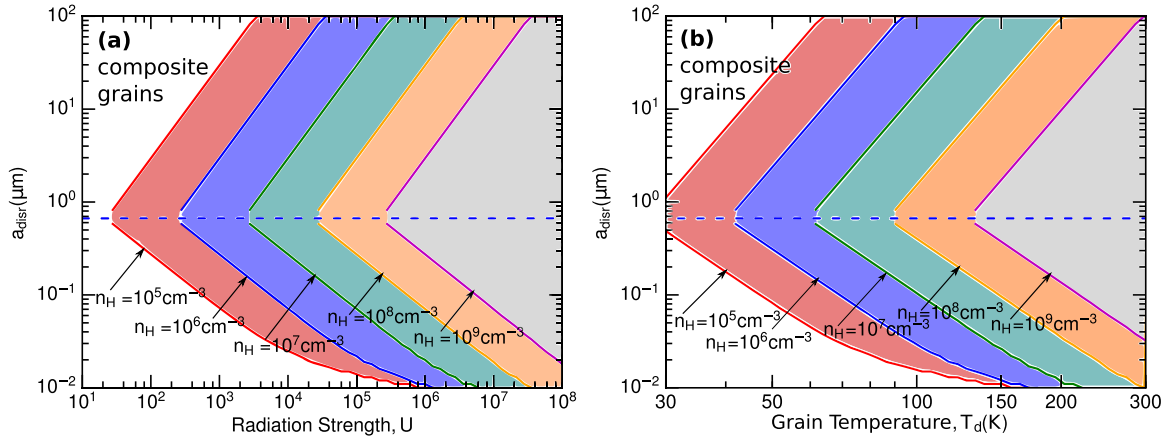

Figure 10. Disruption sizes of composite grains as a function of radiation strength (left panel) and grain temperature estimated at $a = 0.1$ μm (right panel). Composite grains of $a \sim 0.3$–3 μm can be disrupted at temperatures $T_d < 50$ K at density $n_{\rm H} \lesssim 10^6$ cm^{-3}, but for very dense and cold regions ($n_{\rm H} > 10^9$ cm^{-3}, $T_d < 100$ K) very large grains can survive.

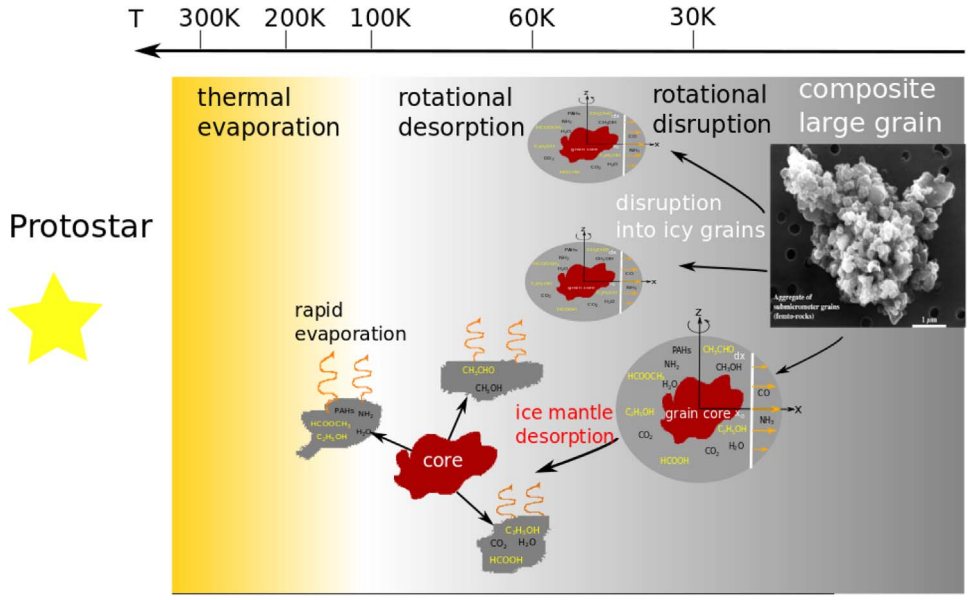

Figure 11. A schematic illustration of dust evolution near a young stellar object. A big composite grain is first disrupted into icy individual grains and there is a subsequent desorption of ice mantles into tiny fragments, which are rapidly evaporated. The formation of COMs and water vapor is thus accompanied by the destruction of large dust grains.

Hoang 2019). Experimental data show a wide range of the tensile strength for aggregate grains, from 10^4 to 10^6 erg cm^{-3}, depending on the particle radius (Gundlach et al. 2018). Thus, for our calculations, we assume the tensile strength $S_{\rm max} \sim 10^5$ erg cm^{-3} which corresponds to the average particle radius $a_p = 10$ nm, assuming a porosity of 20% (see Hoang 2019).

Figure 10 shows the disruption sizes of composite grains in which the maximum size is set to 100 μm and the mean wavelength of the radiation spectrum $\bar{\lambda} = 1.2$ μm. In strong radiation fields ($U \sim 10^3$–10^8) near protostars, large aggregate grains can be rapidly disrupted into smaller grains with ice mantles. The range of the disruption size broadens when the tensile strength is lower because $a_{\rm disr} \propto S_{\rm max}^{-1/2}$ (see Equations (11) and (12)). One notes that in dense and cold regions (e.g., $n_{\rm H} \gtrsim 10^9$ cm^{-3} and $T_d < 100$ K), rotational disruption is inefficient for large grains ($a \gtrsim 1$ μm), such that grain coagulation to planetesimals is not affected by RATD. In this picture, we expect the maximum grain size is larger for dense conditions and weaker radiation fields.

Figure 11 illustrates the evolution of composite grains near a YSO, starting with the disruption into small icy grains and subsequent desorption of the ice mantles into tiny ice fragments. The final stage involves rapid evaporation of mantle species into the gas phase due to higher temperatures of smaller grains by thermal spikes as well as the lower melting temperatures.

In the rotational desorption paradigm, the release of COMs from ice mantles is accompanied with the variation of dust properties as a result of RATs. Thus, rotational desorption implies a correlation between complex molecules and dust properties (e.g., grain size distribution) because the intense radiation field that disrupts the ice mantles also disrupts large

dust aggregates due to their low tensile strength.[5] This effect has a unique signature on observations. First, we expect the increased abundance of COMs corresponds to the reduction of large dust grains, which implies lower opacity at mm–cm wavelengths. Second, the depletion of large aggregate grains results in the change in the polarization pattern because very large grains are expected to experience efficient self-scattering (Kataoka et al. 2015), whereas smaller ones are aligned along the radiation direction or magnetic field direction (Lazarian & Hoang 2007a, 2019; Hoang & Lazarian 2016; Tazaki et al. 2017).

5.4. Rotational Desorption, COMs, Snow Line, and Dust Properties in PPDs

PPDs have layer structures where the gas density increases from $n_{\rm H} \sim 10^5\,{\rm cm}^{-3}$ in the disk atmosphere to $n_{\rm H} \sim 10^{12}\,{\rm cm}^{-3}$ in the disk plane. The gas corresponding temperature is $T \sim 1500$ K to $T \sim 10$ K in the disk plane (see e.g., Figure 12 in Hoang et al. 2018b). Therefore, we expect the rotational desorption to be efficient in the disk surface and intermediate layer where the density $n_{\rm H} < 10^{10}\,{\rm cm}^{-3}$ and $T > 100$ K. The proposed mechanism can explain the detection of COMs in PPDs (Walsh et al. 2014; Favre et al. 2018) as well as in protostellar disks (Lee et al. 2017).

Furthermore, the sublimation of water ice occurs at $T \gtrsim 150$ K, which defines the snow line. At this temperature, we show that ice mantles could already be disrupted into smaller fragments, resulting in subsequent evaporation into water vapor, providing that the local gas density is $n_{\rm H} \lesssim 10^7\,{\rm cm}^{-3}$ (see Figure 5). As a result, water vapor can be observed in regions more extended than the traditional snow line of PPDs as constrained by water ice sublimation. As found in Tung & Hoang (2020), the new snow line described by rotational desorption is more extended than the classical one in the surface and intermediate layer of PPDs.

The present rotational mechanism can explain both the detection of COMs in low temperatures around PPDs and some correlation between dust polarization and COMs by ALMA (Podio et al. 2019). The authors found that the inner edge of H_2CO emission coincides with the location where the dust polarization pattern changes from parallel to the short axis to azimuthal direction, which is explained by polarization due to self-scattering by very large grains (Bacciotti et al. 2018). Moreover, the H_2CO abundance peaks at the edge of mm-dust emission, revealing that H_2CO may be increased due to the decrease of very large grains. Here, we suggest that large grains of $a \sim 10$–$100\,\mu$m are likely reduced from the location of H_2CO emission because of the decrease of gas density that facilitates RATD, such that self-scattering is reduced. But smaller grains can be radiatively aligned with the radiation direction (Lazarian & Hoang 2007a; Hoang & Lazarian 2016), producing an azimuthal polarization pattern (Tazaki et al. 2017).

6. Summary

We studied the effect of suprathermal rotation of grains on the desorption of ice mantles and COMs from grain surfaces in the environs of YSOs. Our principal results are summarized as follows:

1. We showed that in the intense radiation of YSOs, the entire ice mantle can be disrupted into small fragments due to centrifugal force induced by extremely fast rotation of irregular grains spun up by RATs. Thus, icy grain mantles would be removed before the grains can be heated to the ice sublimation temperatures of $T_d \gtrsim 100$ K.
2. We discussed the consequence of resulting fragments and find that the icy fragments of sizes $a \lesssim 10$ Å are heated to high temperatures by single UV photons, triggering transient sublimation of COMs from the fragment. For larger fragments ($a > 10$ Å), thermal sublimation of COMs and water molecules is significantly enhanced compared to sublimation from the original grain because of the increase of grain temperature with decreasing grain size.
3. We identified some key difference between rotational desorption and classical thermal sublimation of COMs that can be tested with observations. We find that rotational desorption can be efficient at temperatures at least ∼20–40 K below the thermal sublimation threshold of COMs.
4. We applied the rotational desorption mechanism to study desorption of COMs in hot cores/corinos. We found that rotational desorption is efficient at much larger distances than thermal evaporation. This can successfully explain the observed COMs in cold, extended regions around high-mass/low-mass protostars.
5. We suggested that the observed enhancement of COMs in the outflow cavity walls could be induced by the rotational desorption mechanism due to irradiation of protostars through the outflow cavity and lower gas density compared to the disk regions. Rotational desorption is also important in the outflows of protostars and PDRs.
6. We found that large aggregate grains that are presumably formed by coagulation in dense regions can be disrupted into distinct grains hosting ice mantles. Such icy grain mantles are then subsequently disrupted into smaller fragments, followed by rapid evaporation of COMs and water ice. Thus, we predict a correlation between COMs and the depletion of large grains in dense regions with strong radiation fields of YSOs.
7. We discussed the implications of rotational desorption of ice mantles in PPDs. Due to rotational desorption, the snow line of PPDs is expected to be more extended than determined by classical thermal sublimation. The observed correlation of COMs and dust polarization can also be explained by rotational desorption mechanism.

We are grateful to the anonymous referee for helpful comments that improved our manuscript. We thank Woojin Kwon for useful comments and suggestions. This work was supported by the National Research Foundation of Korea (NRF) grants funded by the Korea government (MSIT) through the Basic Science Research Program (2017R1D1A1B03035359) and Mid-career Research Program (2019R1A2C1087045). T.L.N. is funded by the SOFIA Postdoctoral fellowship.

[5] The time difference between the disruption of aggregates and the desorption of ice mantles is rather short compared to the age of YSOs (years versus Myrs; see, e.g., Equation (13)). Therefore, in terms of observations, there would be no difference in the observing time of these effects.

ORCID iDs

Thiem Hoang https://orcid.org/0000-0003-2017-0982
Le Ngoc Tram https://orcid.org/0000-0002-6488-8227

References

Andersson, B.-G., Lazarian, A., & Vaillancourt, J. E. 2015, ARA&A, 53, 501
Bacciotti, F., Girart, J. M., Padovani, M., et al. 2018, ApJL, 865, L12
Beltran, M. T., & Rivilla, V. M. 2018, arXiv:1806.08137
Bertin, M., Romanzin, C., Doronin, M., et al. 2016, ApJL, 817, L12
Bisschop, S. E., Jørgensen, J. K., van Dishoeck, E. F., & de Wachter, E. B. M. 2007, A&A, 465, 913
Blake, G. A., Sutton, E. C., Masson, C. R., & Phillips, T. G. 1987, ApJ, 315, 621
Bottinelli, S., Ceccarelli, C., Lefloch, B., et al. 2004, ApJ, 615, 354
Brown, P. D., Charnley, S. B., & Millar, T. J. 1988, MNRAS, 231, 409
Chandler, C. J., & Richer, J. S. 2000, ApJ, 530, 851
Charnley, S. B., Tielens, A. G. G. M., & Millar, T. J. 1992, ApJL, 399, L71
Chokshi, A., Tielens, A. G. G. M., & Hollenbach, D. 1993, ApJ, 407, 806
Chrysostomou, A., Hough, J. H., Whittet, D. C. B., et al. 1996, ApJL, 465, L61
Collings, M. P., Anderson, M. A., Chen, R., et al. 2004, MNRAS, 354, 1133
Cuppen, H. M., Walsh, C., Lamberts, T., et al. 2017, SSRv, 212, 1
Draine, B. T. 2011, Physics of the Interstellar and Intergalactic Medium (Princeton, NJ: Princeton Univ. Press)
Draine, B. T., & Fraisse, A. A. 2009, ApJ, 696, 1
Draine, B. T., & Lazarian, A. 1998, ApJ, 508, 157
Draine, B. T., & Li, A. 2001, ApJ, 551, 807
Draine, B. T., & Weingartner, J. C. 1996, ApJ, 470, 551
Draine, B. T., & Weingartner, J. C. 1997, ApJ, 480, 633
Drozdovskaya, M. N., Walsh, C., Visser, R., Harsono, D., & van Dishoeck, E. F. 2015, MNRAS, 451, 3836
Favre, C., Fedele, D., Semenov, D., et al. 2018, ApJL, 862, L2
Fayolle, E. C., Oberg, K. I., Garrod, R. T., van Dishoeck, E. F., & Bisschop, S. E. 2015, A&A, 576, A45
Garrod, R. T. 2013, ApJ, 765, 60
Garrod, R. T., & Pauly, T. 2011, ApJ, 735, 15
Garrod, R. T., Widicus Weaver, S. L., & Herbst, E. 2008, ApJ, 682, 283
Godard, B., Pineau des Forêts, G., Lesaffre, P., et al. 2019, A&A, 622, A100
Greenberg, J. 1989, in IAU Symp. 135, Interstellar Dust, ed. L. J. Allamandola & A. G. G. M. Tielens (Dordrecht: Kluwer), 345
Greenberg, J. M., Mizutani, H., & Yamamoto, T. 1995, A&A, 295, L35
Gundlach, B., Schmidt, K. P., Kreuzig, C., et al. 2018, MNRAS, 479, 1273
Hasegawa, T. I., & Herbst, E. 1993, MNRAS, 261, 83
Herbst, E., & van Dishoeck, E. F. 2009, ARA&A, 47, 427
Herranen, J., Lazarian, A., & Hoang, T. 2019, ApJ, 878, 96
Hirashita, H., & Li, Z.-Y. 2013, MNRAS, 434, L70
Hoang, T. 2019, ApJ, 876, 13
Hoang, T., Cho, J., & Lazarian, A. 2018a, ApJ, 852, 129
Hoang, T., Draine, B. T., & Lazarian, A. 2010, ApJ, 715, 1462
Hoang, T., Lan, N. Q., Vinh, N. A., & Kim, Y.-J. 2018b, ApJ, 862, 116
Hoang, T., & Lazarian, A. 2008, MNRAS, 388, 117
Hoang, T., & Lazarian, A. 2009, ApJ, 695, 1457
Hoang, T., & Lazarian, A. 2016, ApJ, 831, 159
Hoang, T., & Tram, L. N. 2019, ApJ, 877, 36
Hoang, T., Tram, L. N., Lee, H., & Ahn, S.-H. 2019, NatAs, 3, 766
Hoang, T., & Tung, N. D. 2019, ApJ, 885, 125
Itagaki, K. 1983, US Army Cold Regions Research and Engineering Laboratory CRREL-8326
Jimenez-Serra, I., Vasyunin, A. I., Caselli, P., et al. 2016, ApJL, 830, L6
Karska, A., Kristensen, L. E., van Dishoeck, E. F., et al. 2014, A&A, 572, A9
Kataoka, A., Muto, T., Momose, M., et al. 2015, ApJ, 809, 78
Kim, S.-H., & Martin, P. G. 1995, ApJ, 444, 293
Kwon, W., Looney, L. W., Mundy, L. G., Chiang, H.-F., & Kemball, A. J. 2009, ApJ, 696, 841
Lazarian, A., Andersson, B.-G., & Hoang, T. 2015, in Polarimetry of Stars and Planetary Systems, ed. L. Kolokolova, J. Hough, & A.-C. Levasseur-Regourd (New York: Cambridge Univ. Press), 81
Lazarian, A., & Hoang, T. 2007a, MNRAS, 378, 910
Lazarian, A., & Hoang, T. 2007b, ApJL, 669, L77
Lazarian, A., & Hoang, T. 2019, ApJ, 883, 122
Lee, C.-F., Li, Z.-Y., Ho, P. T. P., et al. 2017, ApJ, 843, 27
Lefloch, B., Ceccarelli, C., Codella, C., et al. 2017, MNRAS, 469, L73
Li, A., & Greenberg, J. M. 1997, A&A, 323, 566
Litwin, K. L., Zygielbaum, B. R., Polito, P. J., Sklar, L. S., & Collins, G. C. 2012, JGRE, 117, E08013
Mathis, J. S., Mezger, P. G., & Panagia, N. 1983, A&A, 128, 212
Mathis, J. S., Rumpl, W., & Nordsieck, K. H. 1977, ApJ, 217, 425
Mumma, M. J., Weissman, P. R., & Stern, S. A. 1993, in Protostars and Planets III, ed. E. H. Levy et al. (Tucson, AZ: Univ. Arizona Press), 1177
Nomura, H., & Millar, T. J. 2004, A&A, 414, 409
Oberg, K. I., Bottinelli, S., Jørgensen, J. K., & van Dishoeck, E. F. 2010, ApJ, 716, 825
Oberg, K. I., Linnartz, H., Visser, R., & van Dishoeck, E. F. 2009, ApJ, 693, 1209
Ossenkopf, V. 1993, A&A, 280, 617
Ossenkopf, V., & Henning, T. 1994, A&A, 291, 943
Pagani, L., Steinacker, J., Bacmann, A., Stutz, A., & Henning, T. 2010, Sci, 329, 1622
Palau, A., Walsh, C., Sánchez-Monge, Á, et al. 2017, MNRAS, 467, 2723
Pauly, T., & Garrod, R. T. 2016, ApJ, 817, 146
Podio, L., Bacciotti, F., Fedele, D., et al. 2019, A&A, 623, L6
Purcell, E. M. 1979, ApJ, 231, 404
Roberge, W. G., & Lazarian, A. 1999, MNRAS, 305, 615
Spaans, M., Hogerheijde, M. R., Mundy, L. G., & van Dishoeck, E. F. 1995, ApJL, 455, L167
Tazaki, R., Lazarian, A., & Nomura, H. 2017, ApJ, 839, 56
Tram, L. N., & Hoang, T. 2019, ApJ, 886, 44
Tung, N.-D., & Hoang, T. 2020, ApJ, submitted (arXiv:2002.03390)
van Dishoeck, E. F. 2014, FaDi, 168, 9
van Dishoeck, E. F. 2017, 3, arXiv:1710.05940
Visser, R., Kristensen, L. E., Bruderer, S., et al. 2012, A&A, 537, A55
Viti, S., & Williams, D. A. 1999, MNRAS, 305, 755
Walsh, C., Millar, T. J., Nomura, H., et al. 2014, A&A, 563, A33
Watson, W. D., & Salpeter, E. E. 1972, ApJ, 174, 321
Weingartner, J. C., & Draine, B. T. 2001, ApJ, 548, 296
Whittet, D. C. B., Bode, M. F., Longmore, A. J., Baines, D. W. T., & Evans, A. 1983, Natur, 303, 218
Whittet, D. C. B., Hough, J. H., Lazarian, A., & Hoang, T. 2008, ApJ, 674, 304
Work, A., & Lian, Y. 2018, PrAeS, 98, 1